Noname manuscript No.
(will be inserted by the editor)

Distinct Gaussian Properties of Multiple Reflections in Extended Hemispherical Lenses

Burak Ozbey · Kubilay Sertel

Received: date / Accepted: date

Abstract Multiple reflections in an extended hemispherical lens are shown to exhibit distinctly-different Gaussian characters. It is demonstrated that the second- and third-order bounces of the electromagnetic fields within the electrically-large lens result in contributions with spot sizes and locations that are uncorrelated with the fundamental Gaussian-beam-like radiation from a small antenna located at the lens focus. We present the optical properties (Gaussicities and power levels at the beam waist) of such higher-order lens reflections. The impacts of these reflections on a typical quasi-optical spectroscopy setup are discussed. The relative received power densities are computed and compared with measurements for each higher-order reflection. The agreement between the measurement and theory indicates that the adopted method is a reliable and efficient tool for characterization of the dominant reflections from extended hemispherical lenses.

Keywords Lens-integrated antenna · Double-slot antenna · Extended hemispherical lens · THz time domain spectroscopy (THz-TDS) · Ray tracing

1 Introduction

Lens-integrated antennas offer significant benefits for millimeter-wave (mmW) and terahertz (THz) applications, where a high directivity, high Gaussicity, and minimal spherical aberrations are desired. High directivity implies a collimated radiation, which facilitates the guidance of the electromagnetic energy through a set of lenses and mirrors in an optical or quasi-optical setup which

This work was supported by NSF Division of Elect., Comm, & CyberSystems (EECS-1710977) under the project "Compact polarimetric THz sensor for reflectometric imaging"

B. Ozbey and K. Sertel
The ElectroScience Laboratory, The Ohio State University, Columbus, OH 43212 USA
E-mail: bozbey000@gmail.com, sertel.1@osu.edu

is typically utilized in mmW/THz systems. On the other hand, Gaussicity is also an important measure for such quasi-optical systems where the efficiency of electromagnetic coupling of antenna radiation into the fundamental mode (zeroth-order Gaussian beam) of an optical system is desired. Gaussicity can be defined as the coupling efficiency of the far-field pattern of an antenna to the far-field pattern of a Gaussian beam [1]. As such, it is a measure of the similarity of the antenna pattern to a Gaussian distribution. However, in quasi-optical systems where electrically-large lenses and reflectors are involved, the far-field based definition of Gaussicity in [1] may not be sufficient to evaluate coupling efficiency.

Lens-integrated photoconductive antennas are key enablers of commercial THz time domain spectroscopy (THz-TDS) systems. A typical THz-TDS system consists of a femtosecond laser source as a local oscillator (LO) that drives both the transmitter antenna and the receiver sensor, as illustrated in Fig. 1. Planar photoconductive antennas are placed at the focal plane of an extended hemispherical lens and a photoconductive switch is triggered by the ultrashort pulses of the LO laser, creating ultra-fast surface current transients on the conductors of the antenna. These currents subsequently lead to pulses of electromagnetic energy with a THz spectrum, typically spanning 60GHz-5THz. The energy radiated by the planar photoconductive antenna is collimated by the lens and coupled to a quasi-optical system that guides the THz energy through the sample under test and onto the receiver antenna. Parabolic reflectors are preferred in such systems due to their much lower losses.

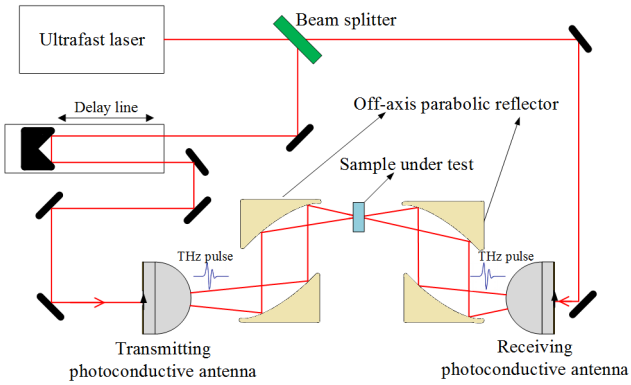

Fig. 1 A typical THz time domain spectroscopy setup employing extended hemispherical lens-integrated antennas as the photoconductive transmitter/receiver of THz pulses.

The extended hemispherical lens structure has proven extremely useful as it can be tuned to effectively couple into a wide range of optical systems, simply by adjusting the extension length, L [1, 2]. Also, various planar antenna topologies can be incorporated into the lens. Among such alternatives

are dipole, double-dipole, spiral or log-periodic topologies [3–7]. Perhaps the most popular antenna geometry is the double-slot antenna [8–12]. Filipovic et al. studied the double-slot antenna structure extensively in [1] and [2], and developed a ray-optics/field integration-based method to calculate the radiation patterns and Gaussian-coupling efficiencies of a double-slot antenna on a hemispherical lens with varying the extension length. However, a key simplification in their analysis was the omission of the multiple internal reflections within the lens structure. In [13–15], the authors examined the effects of the internal reflections in elliptical lenses integrated with various antenna geometries and concluded that for large observation angles, both the co-polar and cross-polar patterns are significantly impacted. In [16], Wu et al. analyzed the effects of internal reflections on the radiation pattern of an ellipsoidal lens excited by a circularly polarized rectangular patch, where the lens material had a relatively lower dielectric constant (Rexolite, $\epsilon_r = 2.54$). Although the inclusion of the multiple reflections affected the computed antenna radiation pattern, these changes were limited to only after the third sidelobe, which is typically 25 dB lower than the main beam [16].

In fact, the reflections in the extended hemispherical lenses can be more detrimental when a higher index material, such as Silicon is used. Moreover, accurate characterization of the electromagnetic near-fields is essential for mmW and THz applications where the focusing properties of the antenna beam impacts the quasi-optical coupling of the signal as well as the position and quality of the virtual foci within the optical sub-system. For instance, for the simple THz-TDS setup shown in Fig. 2(a), first-order fields radiated by the transmitting antenna are collimated by the lens. As such, the relative positions of the lenses and the off-axis parabolic reflectors are not important as long as both the lens and the mirror stay aligned to the optical axis. This collimated beam is the desired behavior since it can couple well to the optical system. However, a significant part of the first-order antenna radiation is reflected back into the lens from the lens-air boundary. The reflected energy then creates a virtual focus (at the complementary focal point of the ellipse), and subsequently reflects back from the antenna plane toward the spherical lens surface. As illustrated in Fig. 2(b), this second-order transmission does not have the same collimated form as the first-order transmission. As such, the second-order beam now exhibits a virtual focus just outside the lens surface. That is, the location of the off-axis mirror directly impacts the collimation and focusing propeties of the second-order transmitted beam. For the second-order fields, not only the illumination of the sample under test is unfocused, but also the beam reaching the receiver is not aligned with its quasi-optical receiving mode.

We must note, however, that this second-order signal arrives at the receiver at a later time, as it is delayed by the optical path within the lens. In a wideband system, such as pulsed THz-TDS, this second-order signal can be "time-gated" and removed via subsequent signal processing. However, for continuous wave (CW) applications, this is not possible. Therefore, the effects of multiple internal reflections within the lens should be analyzed more rig-

orously for a complete characterization of these internal bounces, particularly when high-index lens materials are used.

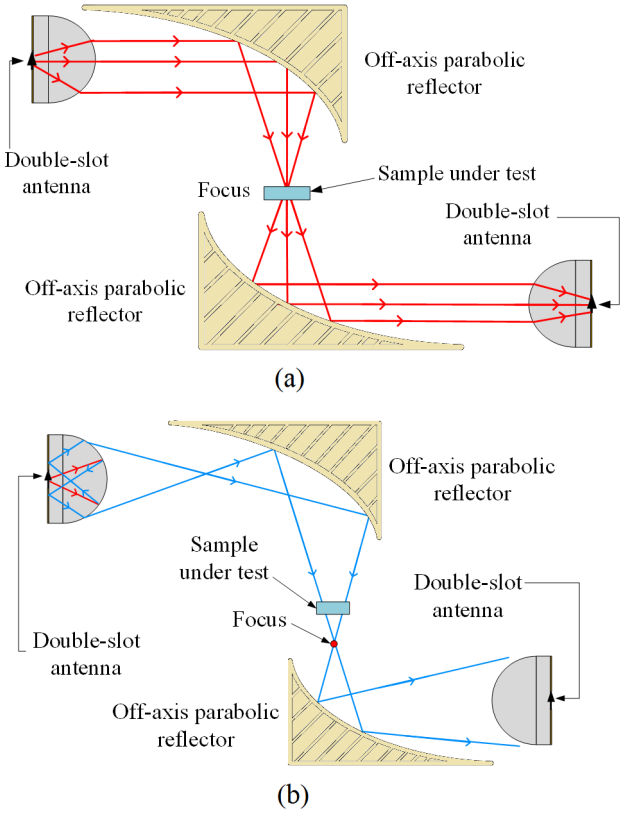

Fig. 2 A simple THz-TDS setup with two extended hemispherical lens-integrated antennas and two off-axis parabolic reflectors: (a) First order transmission (collimated), (b) Second order transmission (uncollimated).

Here, we first present a ray-tracing-based analysis of the effects of multiple internal reflections within an extended hemispherical lens integrated with a planar double-slot antenna structure. The propagation, multiple reflection and transmission effects are analyzed to compute optical parameters such as Gaussian beam waist radius and location with respect to the lens. Electromagnetic wave behavior inside the lens, as well as over a large region outside the lens are computed using the first- and second-order effects. The second-order reflections, i.e., internal reflections from the lens-air boundary and the focal plane, as well as the cylindrical extension are taken into account in the calculations. The results show that the inclusion of the second-order transmission produces better agreement with measurements of the antenna far-field pattern, as also have been reported in [13–15]. After this verification, we analyze

the dominant reflections from an extended hemispherical lens with a ground plane with a focus on their effects on received signal quality in THz-TDS. We characterize the three dominant reflected fields for a quasi-optical link formed by the lens, an off-axis parabolic reflector and a horn antenna. The computed results for the received power are shown to agree with those from the measurements performed on the actual system, validating that the signal from the second-order transmission can be significant, which could adversely affect the overall performance of CW spectroscopy systems. The third dominant reflection, which is produced after multiple internal reflections, is also shown to have a significant power level, as verified by the measured data.

The organization of this paper is as follows: Section 2 presents the problem of multiple internal reflections in extended hemispherical lenses. We employ a ray tracing-based high-frequency analysis, in which the equivalent surface current densities are used to calculate the electromagnetic fields inside and outside the electrically-large extended hemispherical lens. In Section 3, the computational results are presented, and the Gaussian beam properties of the first- and second-order transmissions are discussed. In Section 4, the computed antenna radiation patterns are compared to previous works and measured data. In Section 5, the three most dominant reflections from a lens illuminated by a plane wave are analyzed for an optical link of a reflector and a horn antenna and compared to measurement results. Finally, we summarize our conclusions in Section 6.

2 High-frequency Modeling of Wave Propagation within an Extended Hemispherical Lens

Commercially available full-wave electromagnetic solvers are quite effective in modeling a wide range of practical antenna designs. However, the electrically-large size of a typical lens-integrated antenna requires extensive computational sources for full-wave solvers, thus, their utility as a design tool is limited and often not practical. In particular, for mmW and THz-frequency applications, the lens diameter is typically in excess of tens of wavelengths inside the lens material. In addition, the lens is often made of a high dielectric constant material, requiring a very fine discretization to capture its electromagnetic behavior accurately. Alternatively for uniform material lenses, the problems can be treated using surface equivalence, and the conventional Poggio-Miller-Chan-Harrington-Wu-Tsai (PMCHWT) formulation [17] using equivalent electric and magnetic surface currents can be employed for a succinct representation of the problem. However, as noted above, the numerical solution of this surface integral equation still requires prohibitively-large computational resources due to the large electrical size of the lens. In addition, the integration of the lens with the antenna creates further subtleties in the numerical modeling, often impacting the convergence of the particular iterative solver used. Thus, an alternative computational analysis that can provide a fast, albeit approximate, solution of such an electrically-large problem is needed.

A diagram of a typical extended hemispherical lens integrated with a double-slot antenna is illustrated in Fig. 3. The 3-dimensional (3D) view of the problem with the necessary geometrical quantities is shown in Fig. 3(a). The focal plane of the lens with a double-slot antenna at its center is depicted in Fig. 3(b). The analysis procedure employed in this work is an extended version of the ray-tracing and field integration technique adopted by Filipovic et al. in [1] and [2], and later in [16] for a circularly-polarized patch antenna. Initially, the radiation pattern of the double-slot antenna residing in an infinite ground plane between two half-spaces representing the air and lens material regions is computed using a conventional full-wave analysis, such as the moment method. The antenna radiation into the lens half-space is then used to calculate the fields impinging on the internal surface of the lens facing the double-slot antenna. Subsequently, the first-order incident fields travel through the spherical lens interface. To capture this "refraction" and calculate the equivalent surface currents on the outer surface of the lens, Fresnel transmission coefficients defined for the lens-air interface are utilized using the geometrical setup in Fig. 3(a). Consequently, the equivalent currents on the outer surface of the lens radiate the first-order transmitted waves through the lens and constitute the dominant radiation mechanism of the lens-integrated double-slot antenna [1, 2]. However, we note that when the lens material exhibits high dielectric contrast (such as Silicon with $\epsilon_r \sim 11.7$), the first-order fields radiated by the double-slot antenna also experience a significant reflection from the internal lens surface back into the lens material. In [18, 19], we incorporated higher-order reflections into the first-order approximate analysis provided in [1, 2] to capture the impact of the multiple bounces inside the lens on the far-field radiation pattern of the antenna. Here, we consider for the first time the impact of multiple internal reflections on the near-field properties of the reflected and refracted fields, with particular emphasis on the distinct Gaussian character and the focusing behavior of the first- and the second-order bounces. In addition, we analyze the impact of internal lens reflections on the received signal in a quasi-optical THz spectroscopy setting to demonstrate the potential complications in signal quality due to multiple internal reflections. The multi-step procedure employed here can be summarized as follows:

Step 1: First, as noted above, the magnetic currents on the double-slot antenna is used to find the radiation pattern and fields at the lens-air interface. Assuming that the antenna lies on a plane perpendicular to the optical axis (chosen as the z-axis in the following analysis) and the slots are directed along the y-direction, we can represent the magnetic current variation on the slots as $I_m = \sin[I_{max} k_m (l - |y'|)]$, where $k_m = 2\pi\sqrt{\epsilon_m}/\lambda_0$ and $\epsilon_m = (1 + \epsilon_r)/2$, in which ϵ_r is the dielectric constant of the lens material [1, 20]. The vector

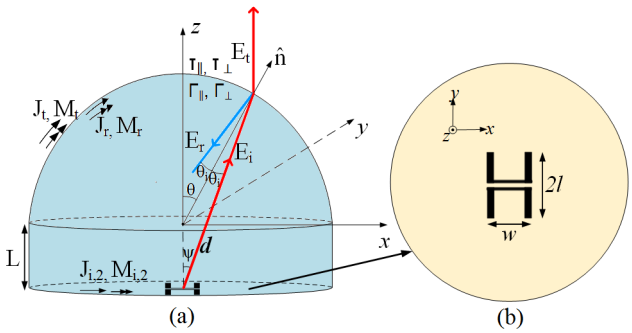

Fig. 3 Geometry of the lens-integrated antenna: A 3-D view of the (a) extended hemispherical lens, and (b) the focal plane of the lens where a double-slot antenna is placed as the feed element (reproduced based on a figure in [2]).

potential $\mathbf{F}$ due to one of the slots is then:

$$\mathbf{F} = \hat{y}\frac{\epsilon_r\epsilon_0}{4\pi}\int_{-l}^{l} I_m(y')\frac{e^{-jk_eR}}{R}dy' \tag{1}$$

$$\simeq \hat{y}\frac{\epsilon_r\epsilon_0 I_{max}e^{-jk_er}}{4\pi r}\int_{-l}^{l}\sin[k_m(l-|y'|)]e^{jk_e\hat{r}\cdot y'\hat{y}}dy' \tag{2}$$

$$= \hat{y}\frac{\epsilon_r\epsilon_0 I_{max}(2k_m)\,e^{-jk_er}}{4\pi r}\frac{\cos(k_el\sin\theta\sin\phi)-\cos(k_ml)}{k_m^2-k_e^2\sin^2\theta\sin^2\phi} \tag{3}$$

Here, k_e is the wavenumber inside the lens. In fact, since the antenna is located at $z=-L$ in the extended hemispherical geometry, the angle θ of spherical coordinates should be replaced with Ψ (as shown in Fig. 3(a)) which can be readily calculated using law of cosines, while ϕ remains unchanged. Moreover, r should also be substituted with $d=|\boldsymbol{d}|$, the magnitude of the vector from the origin of the antenna to the surface of the lens. Doing so, we can also calculate $\mathbf{F}_{\rm ds}$, the vector potential due to the double-slot geometry as the product of $\mathbf{F}$ with the array factor AF:

$$\mathbf{F}_{\rm ds} = \hat{y}\frac{\epsilon_r\epsilon_0 F_0\,e^{-jk_ed}}{4\pi d}\frac{\cos(k_el\sin\Psi\sin\phi)-\cos(k_ml)}{k_m^2-k_e^2\sin^2\Psi\sin^2\phi}\times\mathrm{AF} \tag{4}$$

where

$$\mathrm{AF} = \cos(k_ew/2\sin\Psi\cos\phi). \tag{5}$$

Assuming an electrically large lens, the electric and magnetic fields impinging on the inside surface of the lens-air interface can then be computed using the far-field approximations:

$$\mathbf{H}\simeq -j\omega\mathbf{F}_{\rm ds},\quad \mathbf{E}=-\eta_e\hat{d}\times\mathbf{H}, \tag{6}$$

where η_e is the intrinsic impedance inside the lens and $\hat{d} = \boldsymbol{d}/|\boldsymbol{d}|$ is the unit vector in the direction of $\boldsymbol{d}$.

Step 2: Fields at the interface are decomposed into parallel and perpendicular polarization components with respect to the plane of incidence, and the Fresnel transmission and reflection coefficients are defined for both polarizations as in [21], assuming a locally plane wave incidence, viz.:

$$\Gamma_{\parallel} = \frac{n\sqrt{1-n^2\sin^2\theta_i} - \cos\theta_i}{n\sqrt{1-n^2\sin^2\theta_i} + \cos\theta_i} \tag{7}$$

$$\tau_{\parallel} = (1+\Gamma_{\parallel})\frac{\cos\theta_i}{\sqrt{1-n^2\sin^2\theta_i}} \tag{8}$$

$$\Gamma_{\perp} = \frac{n\cos\theta_i - \sqrt{1-n^2\sin^2\theta_i}}{n\cos\theta_i + \sqrt{1-n^2\sin^2\theta_i}} \tag{9}$$

$$\tau_{\perp} = 1 + \Gamma_{\perp}, \tag{10}$$

where n is the refractive index given by $n = \sqrt{\epsilon_r}$ and θ_i is the angle of incidence. The transmitted electric field $\mathbf{E}_{\mathrm{t}}$ and the ray vector $\hat{s}$ outside the lens can then be found using $\tau_{\parallel}$ and $\tau_{\perp}$, as described in [2]. Reflected electric field $\mathbf{E}_{\mathrm{r}}$ and the reflected ray vector $\hat{s}_r$ can also be found similarly using $\Gamma_{\parallel}$ and $\Gamma_{\perp}$. Assuming plane wave propagation, magnetic field just outside and inside the lens is given as

$$\mathbf{H}_{\mathrm{t}} = \frac{1}{\eta}\hat{s} \times \mathbf{E}_{\mathrm{t}}, \quad \mathbf{H}_{\mathrm{r}} = \frac{1}{\eta}\hat{s}_r \times \mathbf{E}_{\mathrm{r}}. \tag{11}$$

We note that total internal reflection occurs for incidence angles greater than a critical angle $\theta_{i,c} > \sin^{-1}(1/n)$. Therefore, at these incidence angles, $|\Gamma_{\parallel}| = |\Gamma_{\perp}| = 1$ and $\tau_{\parallel} = \tau_{\perp} = 0$.

Step 3: Equivalent surface current densities are calculated at the lens-air interface, viz.:

$$\mathbf{J}_{\mathrm{t}} = \hat{n} \times \mathbf{H}_{\mathrm{t}}, \quad \mathbf{M}_{\mathrm{t}} = -\hat{n} \times \mathbf{E}_{\mathrm{t}} \tag{12}$$

$$\mathbf{J}_{\mathrm{r}} = \hat{n} \times \mathbf{H}_{\mathrm{r}}, \quad \mathbf{M}_{\mathrm{r}} = -\hat{n} \times \mathbf{E}_{\mathrm{r}} \tag{13}$$

where, $\mathbf{J}_{\mathrm{t}}$ and $\mathbf{M}_{\mathrm{t}}$ are used to find the transmitted fields and $\mathbf{J}_{\mathrm{r}}$ and $\mathbf{M}_{\mathrm{r}}$ are used to find the fields reflected back into the lens.

Step 4: The equivalent surface current densities calculated in Step 3 are used in Huygens' integrals to find the fields reflected from and transmitted through the interface. For evaluating the integrals, the Stratton-Chu formulation is preferred in order to calculate the fields everywhere instead of just in the far-field region. In addition, the gradient of the 3D Green's function is defined at the source region such that the integration is straightforward to perform. The Stratton-Chu formulation is given in the form [22]:

$$\begin{aligned}\mathbf{E}_{\mathrm{r,t}}(\mathbf{r}) = \oiint_{S'} \{&-j\omega\mu[\hat{n} \times \mathbf{H}(\mathbf{r}')]g(\mathbf{r},\mathbf{r}') + [\hat{n} \cdot \mathbf{E}(\mathbf{r}')]\nabla' g(\mathbf{r},\mathbf{r}') \\ &+ [\hat{n} \times \mathbf{E}(\mathbf{r}')] \times \nabla' g(\mathbf{r},\mathbf{r}')\} dS'\end{aligned} \tag{14}$$

where, $g(\mathbf{r}, \mathbf{r}')$ is the scalar Green's function, viz.:

$$g(\mathbf{r}, \mathbf{r}') = \frac{e^{-jk|\mathbf{r}-\mathbf{r}'|}}{4\pi|\mathbf{r}-\mathbf{r}'|}. \tag{15}$$

If, for instance, the reflected field is desired, then $\mathbf{J}_{\mathrm{r}}$ and $-\mathbf{M}_{\mathrm{r}}$ are substituted for $\hat{n} \times \mathbf{H}(\mathbf{r}')$ and $\hat{n} \times \mathbf{E}(\mathbf{r}')$, respectively.

Step 5: Steps 1-4 are repeated for the side walls of the cylindrical extension by modifying the problem parameters for the cylindrical geometry. Equivalent electric and magnetic surface current densities for the cylinder are used in (14) to find the contribution from the extension.

As seen above, the Steps 3 to 5 can be repeated to find multiple higher-order reflections. For example, the reflections from the focal plane and/or cylindrical walls of the lens can be calculated through applying these steps in succession. The number of the calculated internal bounces can be as many as desired. However, it is important to note here that a new ray diagram should be drawn for each case to find the ray path vectors $\hat{s}$ or $\hat{s}_r$ in (11).

3 Gaussian Beam Characteristics of The First- and Second-Order Transmissions

As a representative frequency, we consider a simple double-slot antenna, integrated with a 13.7-mm-diameter lens and a 2.7-mm extension length, operating at 246 GHz, the same case studied in [1]. The substrate material of both the lens and the cylindrical extension are high-resistivity Silicon with a relative permittivity of $\epsilon_r = 11.7$. At the operation frequency, radius of the lens and the extension length (L) correspond to $20\lambda_d$ and $7.3\lambda_d$, respectively, where $\lambda_d = \lambda_0/\sqrt{\epsilon_r}$ is the wavelength in Silicon. In addition, the slot half length and the distance between the slots, respectively, are $l = 0.48\lambda_d$ and $w = 0.55\lambda_d$.

In Fig. 4(a), the first-order transmitted electric field ($E_{x,i1}$) is the dominant component of the electric field radiated by the double-slot antenna. This is the same as the approximate solution considered in [1] and [2]. The instantaneous electric field traveling from the slot antenna to the lens interface is shown in Fig. 4(b) and follows the ray-picture as expected. In Fig. 4(c), the first-order reflected field $E_{x,r}$ is shown. It is interesting to note that the first-order reflected wave converges to the "conjugate" focal point inside the Silicon lens, which occurs at the middle of the elliptical lens. After passing through this conjugate focus, $E_{x,r}$ continues to diverge before impinging on the focal plane where the slot antenna resides. Subsequently, this internally reflected wave undergoes another reflection from the ground plane of the antenna. Here, for simplicity, we assume that the presence of the double-slot antenna does not significantly alter the first-order reflected wave's reflection from the focal plane. This approximation is justified given that the reception pattern of the double-slot antenna is significantly mismatched with the first-order reflected wave which appears to be originating from the conjugate focus of the lens. The second-order reflected wave from the lens focal plane, denoted as $E_{x,i2}$, is

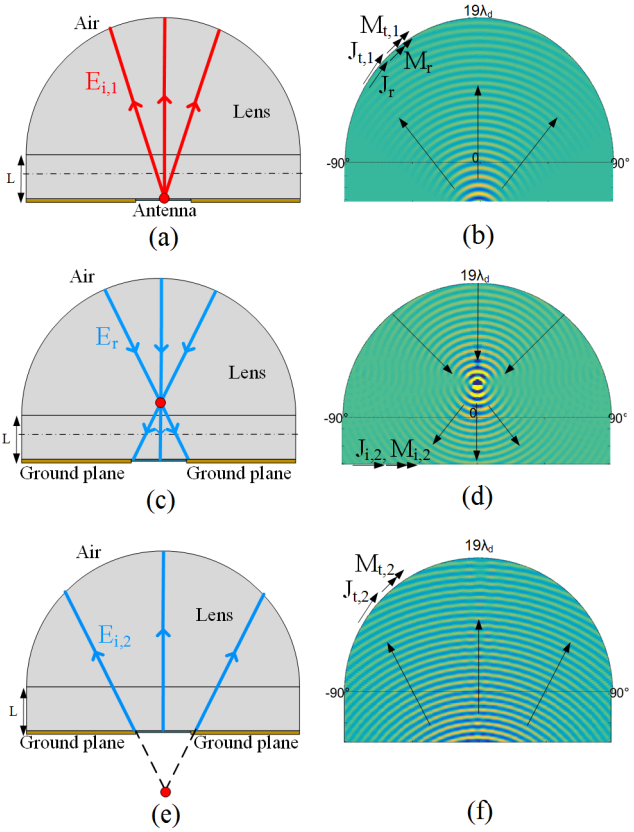

Fig. 4 Incident and reflected instantaneous fields computed inside the extended hemispherical lens. (a)-(b) $E_{x,i1}$: the x component of the first-order incident electric fields on E-plane at a time instant, $t = 0$; (c)-(d) $E_{x,r}$: the x component of the first-order reflected electric field on E-plane at a time instant, $t = 0$; (e)-(f) $E_{x,i2}$: the x component of the second-order incident electric field on E-plane at a time instant, $t = 0$. Ray diagrams are shown on the left hand side and computed fields are shown on the right hand side for each figure.

shown in Fig. 4(e) and (f). The wave reflected from the ground plane is a divergent, non-uniform spherical wave, originating from a fictitious focal point below the antenna ground. However, since the fields are now coming from a more distant focus, the radius of curvature of the wavefronts is larger compared to the first-order radiation from the double-slot antenna which was computed in Step 1. That is, the second-order transmission from the lens-air interface clearly has a different character than the first order field.

The first and second-order transmitted fields outside the lens are shown in Fig. 5 (using a much larger spatial scale). As expected, the first-order transmission, i.e., the field transmitted from the lens-air boundary for the incident wave $E_{x,i1}$, results in a collimated beam, shown in Fig. 5(a). We also note here that the wavelength in air is approximately 3.4-times longer than that in

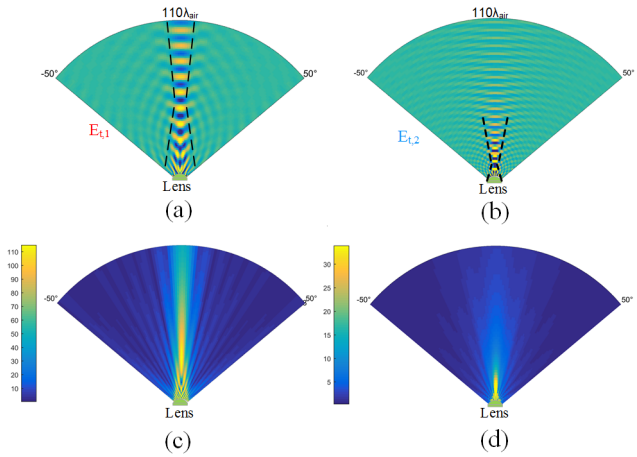

Fig. 5 Computed instantaneous transmitted fields. (a) $E_{x,t1}$, the x component of the first-order transmitted electric field on E-plane at a time instant, $t = 0$, (b) $E_{x,t2}$, the x component of the second-order transmitted electric field on E-plane at a time instant, $t = 0$; (c)-(d) The magnitudes of $E_{x,t1}$ and $E_{x,t2}$.

the lens material. The Gaussian nature of $E_{x,i1}$ can also be clearly observed (as illustrated by the dashed curves in the figure). The beam waist is $1.4\lambda_0$, occurring at $23\lambda_0$ away from the lens surface, where λ_0 is the wavelength in free space, which is 1.22 mm at 246 GHz. In Fig. 5(b), the second-order field transmitted from the lens-air boundary after a complete bounce within the elliptical lens is shown. As seen, the second-order transmission is approximately 3-times lower in magnitude and has completely different Gaussian beam characteristics, as compared to the first-order antenna radiation. Its beam waist is $0.60\lambda_0$, occurring much closer to the lens surface, at approximately $4\lambda_0$ away. As noted before, we remark here again that, the near-field behavior of the first and second-order transmissions are quite dissimilar in their Gaussian character.

4 Effect of Internal Lens Reflections on Antenna Radiation Pattern

When the antenna radiation pattern is concerned, the dramatic effect of the differences in the near field has less, albeit significant, impact. In order to verify the accuracy of the method used, the patterns are first compared to the results of an extended ellipsoid lens demonstrated by Wu et al. in [16]. The extended ellipsoid lens is Rexolite ($\epsilon_r = 2.54$) with radii of 50.0 mm and 38.9 mm for the ellipsoidal and cylindrical parts, respectively. Since this structure is designed to operate at 30 GHz, the lens radius corresponds to about $8\lambda_d$, and can be analyzed via a commercial CAD tool. The antenna is a rectangular patch excited by two slots for circular polarization. The normalized patterns for the ϕ component of the electric field at $\phi = 90°$ plane are presented

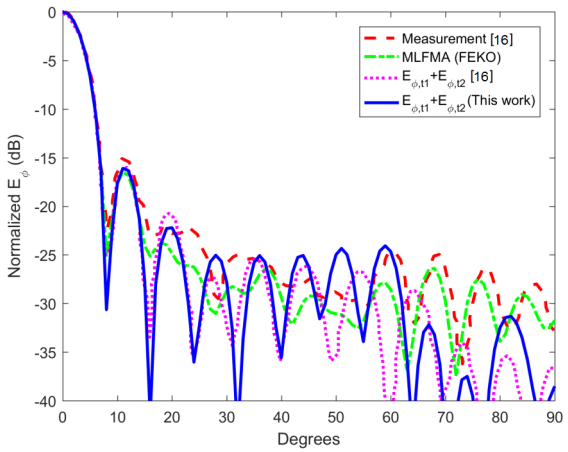

Fig. 6 Radiation pattern at $\phi = 90°$ plane of the ϕ component of the electric field of the circularly polarized patch integrated with an elliposiodal lens [16] at 30 GHz is compared to the patterns obtained by using the method in this work: Measurement [16] (dashed line); full-wave simulation using MLFMA (dash-dotted line); ray tracing algorithm used in [16] (dotted line) and the method used in this work adapted to this problem, H-plane (solid line).

in Fig. 6. Here, the first- and second-order transmissions calculated by the ray tracing algorithm in [16] are compared to the measured and full-wave simulated patterns. The full wave simulation was carried out in FEKO, using the MLFMA acceleration. We also note here the agreement of our method with that given in [16].

Our next example is a high-resistivity Silicon lens integrated with a double-slot antenna operating at 246 GHz. The power levels of the first- and second-order transmissions are shown for the E-plane cut in Fig. 7 for an extension length of $L = 2700$ μm. As seen, while the power difference between $P_{t,1}$ and $P_{t,2}$ is more than 25 dB in the main beam, it is much less at the first, second and third sidelobes, around 12, 10 and 8 dB, respectively. In Fig. 8, the computed and measured patterns (for an extension length of $L = 2700$ μm) are shown for the E-plane cut. Here, the dashed curve represents the patterns obtained by taking only the first-order transmission into account (as in [1]). We note that the result represented by the dashed curve does not take into account the effect of the internal reflections and the cylindrical extension. On the other hand, the dash-dotted curve contains the second-order radiation and the contribution of part of the cylindrical extension, denoted as L_{eff}. Here, $L_{\text{eff}} = 1500$ μm, and the rest of the extension is made of the Silicon wafer, which has a typically much larger radius than that of the lens and thus a negligible contribution to the pattern. The dash-dotted curve should be compared with the solid curve, which is the measurement result given in [1]. Clearly, the inclusion of the second-order internal reflections within the lens yields a better agreement with measurement, more accurately capturing the sidelobes.

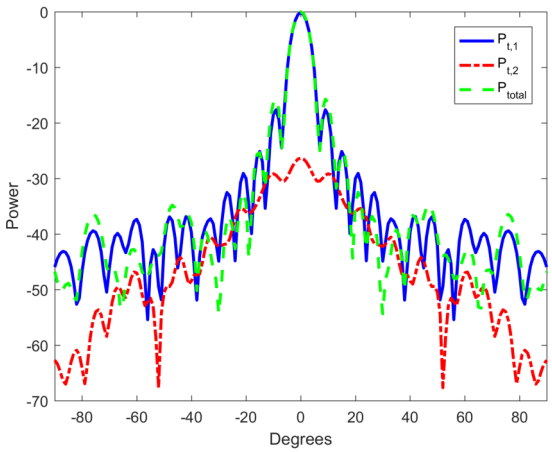

Fig. 7 Power levels of the first- and second-order transmissions of the hemispherical lens-integrated double-slot antenna for an extension of 2700 μm (E-plane).

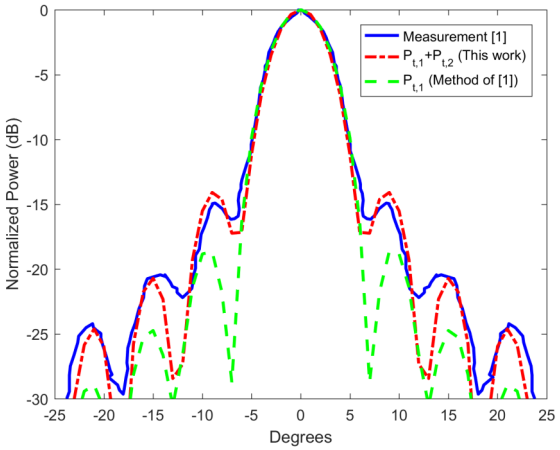

Fig. 8 E-plane radiation patterns for $L = 2700$ μm: Without the contribution of cylindrical extension and second-order transmission (the results in [1] are repeated) (dashed line); with the contribution of the second-order transmission (dash-dotted line) and reflection from the cylindrical extension ($L_{\text{eff}} = 1500$ μm); measurement data (solid line).

5 Effect of Internal Lens Reflections on Time-domain Received Signal

Next, we study the effect of internal lens reflections on a quasi-optical link consisting of a horn antenna, an off-axis parabolic reflector and an extended hemispherical lens, as shown in Fig. 9. This link is part of a typically larger THz time domain spectroscopy setup shown in Fig. 2. First, a Gaussian beam

at 300 GHz is generated by a standard gain diagonal horn antenna. Diagonal horn antennas have a very high Gaussicity ($> 85\%$) [23], and here we assume that the Gaussian beam radiated by the diagonal horn is ideal and has a waist radius of 2.1 mm [24]. The beam impinges on an off-axis parabolic reflector, which serves to collimate the horn radiation. The reflector (modeled after MPD00M9-P01 from Thor Labs, which has a diameter of 12.7 mm) is placed $5r_l$ away from the Silicon lens, where r_l is the radius of the lens (again 6.85 mm). This results in a collimated beam radius of 4 mm. This beam illuminates the hemispherical lens as illustrated in Fig. 9. The beam reflected from the hemispherical surface of the lens is denoted as the first-order reflection, viz., $E_{r,1}$. $E_{r,1}$ is re-focused by the off-axis parabolic reflector as a Gaussian beam. On the other hand, the field which transmits through the lens focuses on the ground plane at the bottom of cylindrical extension ($L = 2.6$ mm for the best approximation of the elliptical lens), gets reflected, and propagates to the lens-air boundary. The reflected field, $E_{r,2}$, is very similar in appearance to the field incident on the focal plane. Part of $E_{r,2}$ then refracts through the air from the Silicon-air boundary. The fraction of $E_{r,2}$ transmitting through the air is focused by the off-axis parabolic mirror, similar to $E_{r,1}$. This field constitutes the second-order reflection captured by the horn antenna shown in Fig. 9. Finally, a third reflection occurs after $E_{r,2}$ is reflected back into the lens and re-transmitted. This reflection, denoted as $E_{r,3}$, constitutes the third most dominant component observed on the spectrum of the reflections from the extended hemispherical lens. For $E_{r,3}$, compared to $E_{r,1}$ and $E_{r,2}$, the field reflected from the mirror does not seem to produce a highly focused beam or a field with Gaussian characteristics. However, as will be shown later, despite being unfocused, the power level of the third order reflection can still be significant. Signal levels of $E_{r,1}$, $E_{r,2}$ and $E_{r,3}$ are computed following the ray tracing algorithm, which is modified to replace the double-slot antenna with a plane wave incident on the lens from its top surface. For these three reflections, the most dominant x-component of the electric fields (according to the coordinate system shown in Fig. 9) are presented in Fig. 10 (a)-(c) for the E-plane cut. The fields reflected from the parabolic off-axis reflector are presented in Fig. 10 (d)-(f) for $E_{r,1}$, $E_{r,2}$ and $E_{r,3}$, respectively.

The most powerful reflections captured by a horn antenna placed at the focus (origin in Fig. 9) of the parabolic mirror are expected to be those that have been analyzed above; namely, the first-, the second- and the third-order reflections. Here, the variations of the power densities for three types of reflections are compared after they are focused by the mirror. The computed variation of the power density along z- and x- for the three reflections with respect to the local coordinates shown in Fig. 9 are plotted in Fig. 11(a) and 11(b), respectively. Here, ρ is the radial component in cylindrical coordinates, defined also with respect to Fig. 9. As seen, the second-order reflection has the highest power level, while the third-order reflection has the least power.

An ideal way to detect the reflections from the lens is to place the antenna at the focal point of the mirror where the energy is spatially most condensed. For collimated reflections ($E_{r,1}$ and $E_{r,2}$), this focal point roughly corresponds

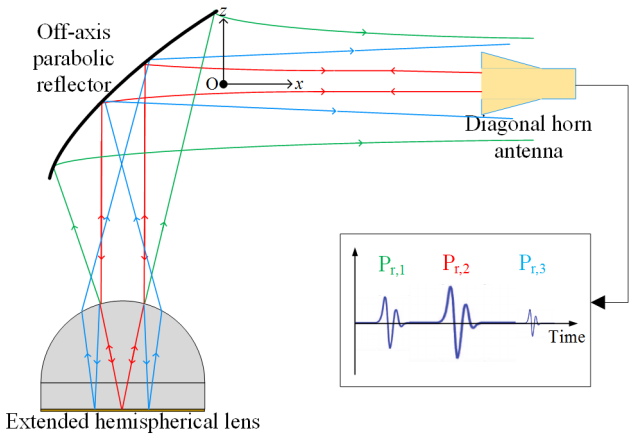

Fig. 9 A quasi-optical link formed by an off-axis parabolic reflector and a horn antenna studied in this work (not to scale). Reflections from the lens which are received by the horn antenna are illustrated in the inset (not actual signals, for illustrative purposes only).

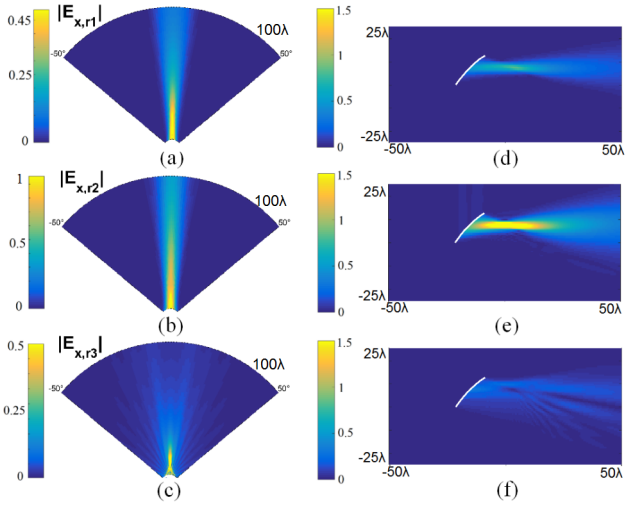

Fig. 10 (a)-(c) x-component of the electric fields (refracting through air from the lens) incident on the off-axis parabolic reflector for $E_{r,1}$, $E_{r,2}$ and $E_{r,3}$ (E-plane cut); (d)-(f) z-component of the electric fields after reflection from the parabolic reflector for E_{r1}, E_{r2} and E_{r3} (E-plane cut).

to the location of the waist of the Gaussian beam produced after the mirror. Here, the near-field Gaussicity defined by Filipovic et al. in [1] is adopted as a tool to compare the power coupled to the diagonal horn antenna placed at the beam waist of the first-, second- and third-order reflections, respectively. Gaussicity values of the z- and x-components of the electric fields calculated for three different diagonal horn antennas having 2.1 mm, 1.9 mm and 1.2

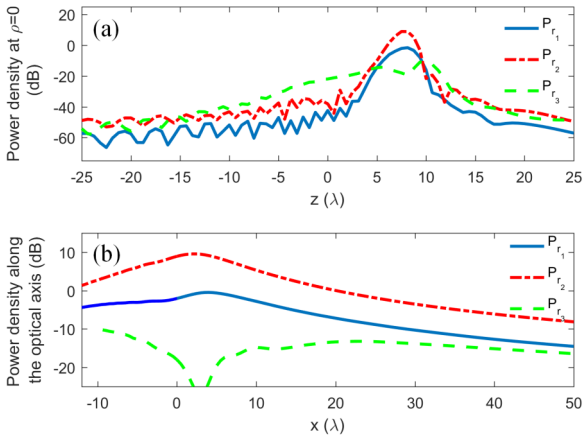

Fig. 11 The power densities for $P_{r,1}$, $P_{r,2}$ and $P_{r,3}$ (a) along z at $\rho = 0$; (b) along x (the optical axis) at $z = 0$, where $\lambda = 1$ mm.

mm beam waist radii, are presented in Table 1. We should note here once again that these values are obtained under the assumption that the incoming beam is perfectly Gaussian, although the actual maximum Gaussicity values for diagonal horn antennas are slightly lower in practice ($\sim 0.8 - 0.9$). As expected, the first and the second order reflected fields have high Gaussicity values, while the third order reflection has much poorer Gaussian coupling efficiency.

Table 1 The computed Gaussicities at the beam waist of the diagonal horn antenna, when the antenna is placed at the beam waist of the reflected fields from the off-axis parabolic mirror ($z = 0, \rho = 0$)

	$w_0 = 2.1$ mm	$w_0 = 1.9$ mm	$w_0 = 1.2$ mm
$E_{r1,z}$	0.93	0.92	0.62
$E_{r1,x}$	0.90	0.90	0.62
$E_{r2,z}$	0.85	0.89	0.76
$E_{r2,x}$	0.77	0.80	0.70
$E_{r3,z}$	0.41	0.36	0.14
$E_{r3,x}$	0.38	0.32	0.11

The modeled time domain system is part of a measurement setup shown in the inset of Fig. 12. Here, the diagonal horn is connected to the vector network analyzer through a waveguide (Keysight N5242A PNA coupled with WR-2.8-band Virginia Diodes Inc. frequency extender), and the optical setup containing the lens and the off-axis parabolic mirror are affixed to the diagonal horn using a 3D printed holder. The only significant additional reflection from such a system apart from those simulated is that from the flange. However, it can easily be distinguished, and it has no effect on the received signal.

The power (normalized with respect to the most dominant reflection, $E_{r,2}$) measured at this setup is shown in dB scale versus time in Fig. 12 for the case when the horn antenna is at the beam waist of $E_{r,2}$. It should be noted that this point is not the focal point for the first- and third-order reflections. However, it is the point where a receiver antenna would have been placed to maximize the collimation of its radiation. Here, the first reflection comes from the flange at zero time (due to VNA calibration), while the rest of the marked peaks correspond to the first-, second- and third-order reflections, respectively. These peaks are compared to the computed values in the figure. The normalized power levels are computed by using the far-field radiation pattern of the diagonal horn antenna given in [25] along with the electric field values at the beam waist of $E_{r,2}$. The measured and computed normalized power levels are also presented in Table 2, which indicates a good agreement.

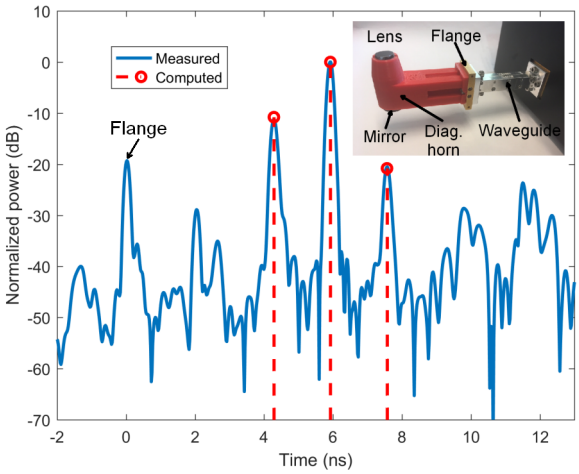

Fig. 12 The measured and computed normalized power for $P_{r,1}$, $P_{r,2}$ and $P_{r,3}$ versus time when the horn is at the beam waist of $P_{r,2}$. The measurement setup is shown at the inset.

Table 2 The measured and computed power values for $P_{r,1}$ and $P_{r,3}$ normalized by $P_{r,2}$, when the horn is at the beam waist of $P_{r,2}$.

	Measured (dB)	Computed (dB)
$P_{r1,n}$	-11.2	-10.8
$P_{r3,n}$	-20.5	-20.8

As discussed before, the position of the parabolic reflector is effective in determining the virtual focus of the reflected waves, especially for the uncollimated reflections from the lens. The change of the power density and Gaussicity are investigated versus a variation in the distance between the lens

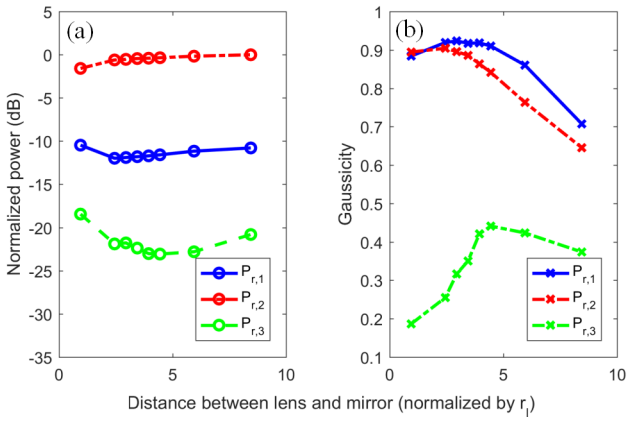

Fig. 13 (a) Variation of computed power densities at the beam waist for $P_{r,1}$, $P_{r,2}$ and $P_{r,3}$ versus d_{lr}, (b) Variation of computed Gaussicities at the beam waist for $P_{r,1}$, $P_{r,2}$ and $P_{r,3}$ versus d_{lr}.

and the parabolic reflector (d_{lr}). The power densities at the focal point of each reflection are shown versus d_{lr} in Fig. 13(a). The Gaussicities are also calculated for each case and are presented in Fig. 13(b) for a varying d_{lr}. It is observed that $P_{r,1}$ and $P_{r,2}$, which are more collimated compared to $P_{r,3}$, exhibit a smaller change in their power levels as compared to the third reflection. This is because the beam that illuminates the hemispherical surface is not an ideal plane wave and its transverse amplitude profile is Gaussian, which results in the collimated reflections largely being confined within the parabolic reflector, almost independent of the change of its position. However, Gaussicity is related with the longitudinal beam profile, and thus, strongly dependent on d_{lr}.

6 Conclusion

We presented a high-frequency analysis of multiple reflections within an extended hemispherical lens with a special focus on their Gaussian characteristics. A ray-tracing-based approach was used to compute the reflected and refracted fields by the lens-air interface and the ground metal at the lens focal plane. The second-order transmitted beam by a lens integrated with a double-slot antenna was shown to exhibit a completely different Gaussian character, with a much smaller beam waist occurring much closer to the lens surface. We also computed the reflected fields using a simple quasi-optical setup consisting of a lens, an off-axis parabolic reflector and a diagonal horn antenna. We showed experimentally that the received power level for each reflection was consistent with measurement result. Our findings indicate that the impact of second-order fields from the lens can be significant, and should be carefully considered. This is particularly important for continuous wave and narrow-

band applications, where it may not be possible to separate such second-order effects through time-gating.

Acknowledgements The lead author would like to thank the Turkish Fulbright Commission for their support under the Postdoctoral Program Grant.

References

1. Filipovic, D.F., Gearhart, S.S., Rebeiz, G.M.: Double-slot antennas on extended hemispherical and elliptical silicon dielectric lenses. IEEE Transactions on Microwave Theory and Techniques **41**(10), 1738–1749 (1993). DOI 10.1109/22.247919
2. Filipovic, D.F., Gauthier, G.P., Raman, S., Rebeiz, G.M.: Off-axis properties of silicon and quartz dielectric lens antennas. IEEE Transactions on Antennas and Propagation **45**(5), 760–766 (1997). DOI 10.1109/8.575618
3. Alder, C.J., Brewitt-Taylor, C.R., Dixon, M., Hodges, R.D., Irving, L.D.: Microwave and millimetre-wave receivers with integral antenna. IEE Proceedings H: Microwaves Antennas and Propagation **138**, 253–257 (1991)
4. Sigel, P.H., Dengler, R.J.: The dielectric-filled parabola: A new millimeter/submillimeter wavelength receiver/transmitter front end. IEEE Transactions on Antennas and Propagation **39**(1), 40–47 (1991)
5. Babakhani, A., Guan, X., Komijani, A., Natarajan, A., Hajimiri, A.: A 77-GHz Phased-Array Transceiver With On-Chip Antennas in Silicon: Receiver and Antennas. IEEE Journal of Solid-State Circuits **41**(12), 2795–2806 (2006)
6. Semenov, A.D., Richter, H., Hubers, H.W., Gunther, B., Smirnov, A., Il'in, K.S., Siegel, M., Karamarkovic, J.P.: Terahertz Performance of Integrated Lens Antennas With a Hot-Electron Bolometer. IEEE Transactions on Microwave Theory and Techniques **55**(2), 239–247 (2007). DOI 10.1109/TMTT.2006.889153
7. Rui, G., Abeysinghe, D.C., Nelson, R.L., Zhan, Q.: Demonstration of beam steering via dipole-coupled plasmonic spiral antenna. Scientific Reports **3**, 2237 (2013). DOI 10.1038/srep02237
8. Bin, M., Gaidis, M.C., Zmuidzinas, J., Phillips, T.G., LeDuc, H.G.: Low-noise 1 THz niobium superconducting tunnel junction mixer with a normal metal tuning circuit. Applied Physics Letters **68**(12), 1714–1716 (1996)
9. Gearhart, S.S., Rebeiz, G.M.: A monolithic 250 GHz Schottky-diode receiver. IEEE Transactions on Microwave Theory and Techniques **42**(12), 2504–2511 (1994). DOI 10.1109/22.339789
10. Chantraine-Bares, B., Sauleau, R., Coq, L.L., Mahdjoubi, K.: A new accurate design method for millimeter-wave homogeneous dielectric substrate lens antennas of arbitrary shape. IEEE Transactions on Antennas and Propagation **53**(3), 1069–1082 (2005)
11. Trichopoulos, G.C., Mumcu, G., Sertel, K., Mosbacker, H.L., Smith, P.: A Novel Approach for Improving Off-Axis Pixel Performance of Terahertz Focal Plane Arrays. IEEE Transactions on Microwave Theory and Techniques **58**(7), 2014–2021 (2010). DOI 10.1109/TMTT.2010.2050175
12. Trichopoulos, G.C., Mosbacker, H.L., Burdette, D., Sertel, K.: A Broadband Focal Plane Array Camera for Real-time THz Imaging Applications. IEEE Transactions on Antennas and Propagation **61**(4), 1733–1740 (2013). DOI 10.1109/TAP.2013.2242829
13. Neto, A., Maci, S., Maagt, P.J.I.d.: Reflections inside an elliptical dielectric lens antenna. IEE Proceedings - Microwaves, Antennas and Propagation **145**(3), 243–247 (1998). DOI 10.1049/ip-map:19981884. URL `https://digital-library.theiet.org/content/journals/10.1049/ip-map_19981884`
14. Vorst, M.J.M.v.d., Maagt, P.J.I.d., Herben, M.H.A.J.: Effect of internal reflections on the radiation properties and input admittance of integrated lens antennas. IEEE Transactions on Microwave Theory and Techniques **47**(9), 1696–1704 (1999). DOI 10.1109/22.788611

15. Vorst, M.J.M.v.d., Maagt, P.J.I.d., Neto, A., Reynolds, A.L., Heeres, R.M., Luinge, W., Herben, M.H.A.J.: Effect of internal reflections on the radiation properties and input impedance of integrated lens antennas-comparison between theory and measurements. IEEE Transactions on Microwave Theory and Techniques **49**(6), 1118–1125 (2001). DOI 10.1109/22.925500
16. Wu, X., Eleftheriades, G.V., Deventer-Perkins, T.E.v.: Design and characterization of single- and multiple-beam mm-wave circularly polarized substrate lens antennas for wireless communications. IEEE Transactions on Microwave Theory and Techniques **49**(3), 431–441 (2001). DOI 10.1109/22.910546
17. Poggio, A.J., Miller, E.K.: Integral equation solutions for three dimensional scattering problems. Pergamon Press, NY (1973)
18. Ozbey, B., Sertel, K.: Effects of internal reflections on the performance of lens-integrated mmW and THz antennas. In: 2018 International Applied Computational Electromagnetics Society Symposium (ACES) (2018). DOI 10.23919/ROPACES.2018.8364149
19. Ozbey, B., Sertel, K.: Reflection characteristics of an extended hemispherical lens for THz time domain spectroscopy. In: 2019 International Workshop on Antenna Technology (iWAT) (2019). DOI 10.23919/ROPACES.2018.8364149
20. Kominami, M., Pozar, D., Schaubert, D.: Dipole and slot elements and arrays on semi-infinite substrates. IEEE Transactions on Antennas and Propagation **33**(6), 600–607 (1985). DOI 10.1109/TAP.1985.1143638
21. Balanis, C.A.: Advanced Engineering Electromagnetics. John Wiley & Sons Inc (1989)
22. Kong, J.A.: Electromagnetic Wave Theory. John Wiley & Sons Inc, New York (1986)
23. Sertel, K., Trichopoulos, G.C.: Non-contact metrology for mm-wave and thz electronics. In: P. Fay, D. Jena, P. Maki (eds.) High-Frequency GaN Electronic Devices, chap. 10, pp. 283–299. Springer, Cham (2019)
24. Virginia Diodes, I.: Nominal Horn Specifications (2006). `http://vadiodes.com/VDI/pdf/VDI%20Feedhorn%20Summary%202006_05.pdf`
25. Johansson, J.F., Whyborn, N.D.: The diagonal horn as a sub-millimeter wave antenna. IEEE Transactions on Microwave Theory and Techniques **40**(5), 795–800 (1992)